

# Terahertz wave emission from mesoscopic crystals of BSCCO

Wei Zhou<sup>1,2</sup>, Chen Wang<sup>1</sup>, and Qing-Hu Chen<sup>2,1,\*</sup>

<sup>1</sup> *Department of Physics, Zhejiang University, Hangzhou 310027, P. R. China*

<sup>2</sup> *Center for Statistical and Theoretical Condensed Matter Physics, Zhejiang Normal University, Jinhua 321004, P. R. China*

(Dated: November 3, 2018)

We study the Terahertz (THz) emission mechanism in BSCCO with an external magnetic field theoretically. The total power is proportional to the square of the number of layers and the frequency. Under the small size limitation, the angular distribution is similar to that in the dipole emission. The present theoretical results for THz power output are in the same order of magnitude as the experimental ones, in contrast with previous simulations. A series of size-dependent intrinsic frequencies are also observed. When the external frequency induced by the external current resonates with intrinsic ones, the distinct THz emission is observed.

PACS numbers: 74.50.+r, 74.25.Gz, 85.25.Cp

Highly anisotropic high-Tc superconductor  $\text{Bi}_2\text{Sr}_2\text{CaCu}_2\text{O}_8$  (BSCCO) is considered as a stack of intrinsic Josephson junctions (IJJs) on atomic scale [1, 2]. This materials may provide a new way to generate terahertz (THz) electromagnetic (EM) wave and therefore possibly fills the "THz gap" [3, 4, 5, 6, 7, 8, 9], one area of the EM spectrum between microwave and infrared frequencies, which has not yet been exploited. The THz EM-wave emission based on AC Josephson effect of IJJs has been detected by Ozyuzer *et al.* [4], and also studied extensively in the theoretical side. Some mechanisms of the THz emission have been proposed [5, 7] recently. However, these mechanisms can not bridge the big gap for the power in simulations [7] and experiments [4, 6].

In this paper, we successfully develop a new boundary conditions, which explains the dipole angular distribution and predicts that the power is proportional to the square of layer number and frequency. By solving the sine-Gordon equations numerically with a proper boundary conditions, we observe a stable power output in some parameter regime. The present power density is in the same order of magnitude as the experimental results. Finally, the detail mechanism is suggested.

The plasma frequency of single Josephson junction is in subterahertz wave band. There is a collective cavity resonance mode in the stack of IJJs, which is crucial to enhance the power and to increase the frequency from sub-THz to THz. IJJ is formed naturally in BSCCO where Bi-Sr-O layers between the superconducting  $\text{CuO}_2$  layers acts as a non-conducting barrier. It can be described by the well known coupled sine-Gordon equation [1]

$$\frac{\partial^2 \phi_{l+1,l}}{\partial x'^2} = (1 - \zeta \Delta^{(2)}) \{ \partial_{t'}^2 \phi_{l+1,l} + \beta \partial_{t'} \phi_{l+1,l} + \sin(\phi_{l+1,l}) \}. \quad (1)$$

where  $x' = x/\lambda_c$  and  $y' = x/\lambda_c$  are the dimensionless positions in the a-b plane,  $t' = \omega_p t$  is the dimensionless time with  $\omega_p = c/\lambda_c \sqrt{\varepsilon_c}$  the Josephson plasma frequency. The current interlayer coupling parameter  $\zeta$  is described as  $\lambda_{ab}^2/sD$ , where  $s$  and  $D$  are the superconducting and

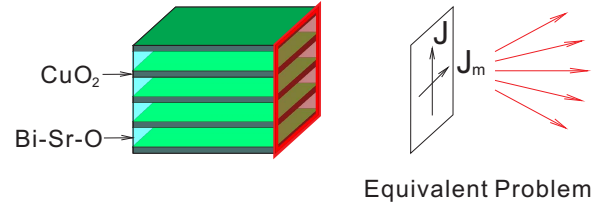


FIG. 1: (Color online). Schematic view of BSCCO source (left) and the equivalent radiation sources (right).

insulating layer thickness.  $\beta = 4\pi\sigma_c\lambda_c/c\sqrt{\varepsilon_c}$  is the resistive dissipation factor, where  $\varepsilon_c$  and  $\sigma_c$  are the dielectric constant and the conductivity of the insulating layers, respectively. The abbreviation operator of  $\Delta^{(2)}$  is defined as  $\Delta^{(2)} f(l) = f(l+1) - 2f(l) + f(l-1)$ .

It is known that the boundary conditions are very crucial for the wave emission. The BSCCO source and outside media region are separated by a boundary surface. On the interface, the surface integrals of  $E$  and  $H$  are constant, except in the red region shown in the Fig. 1. It is an effective radiation section where  $H$  parallel to  $y$ -axis and  $E$  to  $x$ -axis are determined through  $\phi_t = 2eDE_z/\hbar$  and  $\phi_x = 2\pi\mu_0 DH_y/\Phi_0$  respectively. So the EM-wave is described by Maxwell equations outside the BSCCO region and sine-Gordon equations inside the BSCCO region. To evaluate the far field, the original problem could be transformed to an equivalent one described by Love's Formulation [10]. In this way, the original IJJ region is replaced by a free space, the BSCCO source is removed, and equivalent electric and magnetic currents given below are suspended on the boundary surface,

$$J = n \times H,$$

$$J_m = -n \times E,$$

where  $n$  is an unit vector normal to the effective radiation section,  $J$  and  $J_m$  are the equivalent sources producing the same  $E$  and  $H$  in the region outside. According to the superposition principle of the electromagnetic waves,

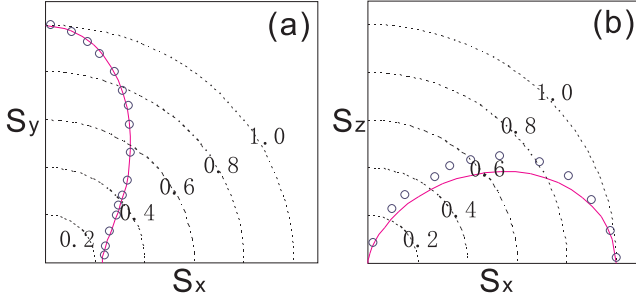


FIG. 2: (Color online). (a) Angular distribution of the radiation energy in ab-plane. The present analytical results are denoted by the solid curve and the previous simulation ones by the open circles. (b) Angular distribution of the radiation energy in ac-plane.

the  $E$  and  $H$  in far field are the sum of contributions from electric sources and magnetic sources respectively. The angular distribution of total power is determined by the radiation from both  $J$  and  $J_m$ . For the electric sources, the vector potential in outside region is generated by  $J$ ,

$$A(r) = \frac{\mu_0}{4\pi} \int dS \int d\omega \frac{J(r', \omega) e^{ik|r-r'| - \omega t}}{|r-r'|}. \quad (2)$$

The average energy flow density can be evaluated by the time averaged Poynting vector

$$\bar{S}(r) = \frac{L_y^2 N_J^2 D^2 \mu_0}{32\pi^2 c} \int d\omega \frac{\omega^2 J^2(\omega)}{r^2} \sin^2 \theta. \quad (3)$$

It is Eq.(3) that can account for a lot of experimental and numerical observations, such as the angular distribution of the emission, total power which is proportional to  $N_J^2$ , and considerable power discrepancies between simulations and experiments.

The analytical results for the angular distribution of the radiation energy by Eq. (3) is plotted in Fig. 2 with the solid curves. Fig. 2(a) shows the results of the xy model with  $L_x = 300\mu m$ ,  $L_y = 100\mu m$ . This model describes the in-phase EM emission from IJJs with infinite junction number. The angular distribution of the  $J_m$  has the cylindrical symmetry, and The angular dependence of  $J$  can be derived from Eq. (2)

$$S_J \propto \left[ \frac{\sin \theta \cos \left( \frac{\pi}{2} \gamma \cos \theta \right)}{(\gamma \cos \theta)^2 - 1} \right]^2, \quad (4)$$

where the  $\gamma = \lambda_h/\lambda = 1.36$ .  $\lambda_h$  is the standing wave length of  $E$  at the boundary, and  $\lambda$  is the wave length of the far field EM wave. Fig. 2(b) shows the radiation in xz-plane of the sample with  $L_x = 100\mu m$  and  $L_z = 0.2\lambda_c$ . The thickness of the source is much smaller than the wave length. Neglecting the  $r'$  in Eq. (2), the Poynting vector is proportional to  $\sin^2 \theta$ , the dipole angular distribution. It is the small size of effective radiation section that generates the dipole angular distribution.

By using a 2D model, Koyama *et al* [9]. simulated the angular distribution of the radiation energy. Their numerical results are also list in Figs. 2(a) and (b) by open circles. It is very interesting that our analytical results agrees quite well with the simulation ones.

It was recently observed that small samples can be used to reduce the heating effect, therefore, the small size approach has been generally adopted. When the EM radiation from the IJJs is approximately monochromatic in THz band, the total power is

$$P = \frac{L_y^2 N_J^2 \omega^2 \Phi_0^2}{96\pi^3 c} \left[ \frac{\phi_x^2}{\mu_0} + \varepsilon_0 \phi_t^2 \right]. \quad (5)$$

When the change of the cavity resonance is not obvious,  $\phi_x(\omega)$  and  $\phi_t(\omega)$  is constant. Thus  $S_{eff}^2 \omega^2 / P$  almost remains unchanged, where  $S_{eff}$  is the area of the effective section. The total power is proportional to the square of the number of layers, consistent with the experimental observations[4].

The power of radiation is also simulated with the uses of the sine-Gordon equations and Eq. (5). Since the magnetic field of the THz EM wave is much smaller than the external one, the boundary condition can be set as  $\phi_{x'} = H'$ ,  $H' = 2\lambda_c DH$ [12]. For such a boundary condition, the Poynting vector can not be calculated directly[13], but Eq. (5) provides another way to the evaluation of the power. The parameters used here are  $\lambda_{ab} = 0.4\mu m$ ,  $\lambda_c = 200\mu m$ ,  $s = 0.3nm$ ,  $D = 1.2nm$ ,  $\beta = 0.02$ ,  $L_x = 20\mu m$  and  $L_y = 20\mu m$ . The number of junctions is  $N_J = 30$ . The power densities obtained in the previous simulations[5, 7] are independent of the effective section area. Lin *et al.*[7] estimated the power density to be around  $400W/cm^2$ , and Tachiki *et al.*[5] about  $3000W/cm^2$ . In sharp contrast with the previous reports, Eq. (5) shows that the power density is proportional to  $S_{eff}$ . Our effective section area is set to  $0.9\mu m^2$ , close to the experimental value[6]. Fig. 3 shows the external current dependence of the power intensity for the external magnetic field  $H_{ext} = 2T$  along the y axis. The blue curve denotes the power averaged from 13.67 ns to 27.34 ns, and the red one from 27.34 ns to 41.01 ns. Because of the appropriate boundary conditions we employed, our result for the power density is much smaller than previous numerical ones reported in the literature[5, 7]. The maximum output for the power density is about  $6W/cm^2$ , which is just in the same order of magnitude as the experimental result observed by Bae *et al.*[6].

Both Figs. 3(a) and (b) have been divided into two different regimes, marked with different background colors. When  $J_{ext} < 0.47J_c$  (in the purple regime), the vortices are randomly distributed. In general, the power roughly increases with  $J_{ext}$ . And if we look into details, it could be found that the blue line and red line do not coincide, due to an unstable power caused by random flux flow. When  $J_{ext} > 0.47J_c$ , the vortex structure is transformed into the in-phase rectangular lattice, a stable configuration. These configurations are discussed analytically by

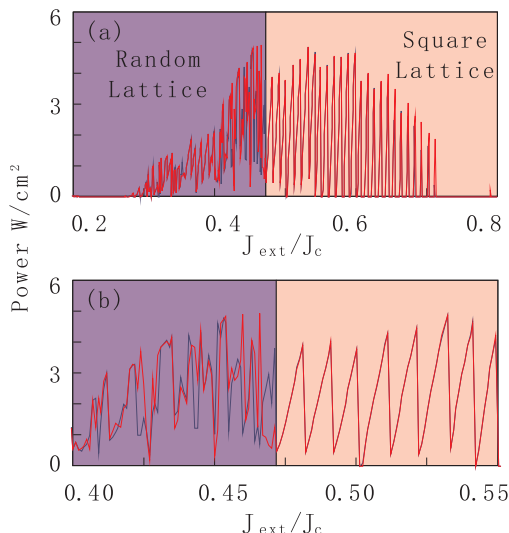


FIG. 3: (Color online). Radiation power as a function of the external current. The blue curve represents the radiation power averaged from 13.67 ns to 27.34 ns, the red curve the radiation power averaged from 27.34 ns to 41.01 ns. (a) In the pink regime, the vortices are distributed almost randomly. In the purple regime, the moving Josephson vortices form the in-phase rectangular lattice. (b) is an enlarged view of (a).

Koshelev[14]. In this situation, the distinct power radiation appears. In addition, the output power fluctuates within the pink regime. This phenomenon is closely related to the radiation mechanism, and will be discussed below.

It is interesting to note that only a small part of the input power, not more than 5%, is able to emit out as EM-wave in all previous experiments [4, 6]. Eq. (5) can give a reasonable explanation to these experimental findings. When  $L_y N_J$  is small, the interior surfaces reflect a wave of low frequencies. The inner EM-wave, generated by AC Josephson effect, bounces back and forth within BSCCO. Like a cavity resonator, where the EM field forms standing waves, the EM waves with resonance frequencies can also form in BSCCO. Every discrete peak in Fig. 3 provides an evidence of the standing waves. Fig. 3(b) is an enlarged view of Fig. 3(a). It is clear that the distances between neighboring peaks are almost the same. These peaks just correspond to the characteristic frequencies with different resonance modes.

The different flux-line lattice structures results in the different V-I curves and frequency characteristics [11]. To understand the resonance mechanism, we analyze the frequency spectra with different external currents. As plotted in the Fig. 4(a) and (b), the frequency spectra of random lattice is much different from that of the rectangular lattice.

Fig. 4(a) shows the frequency spectra with external currents  $J_{ext} = 0.21J_c$ ,  $0.22J_c$  and  $0.23J_c$ . Under these conditions, the output power is less than 1% of the maximum. With low  $J_{ext}$ , the spectra are not monochromatic

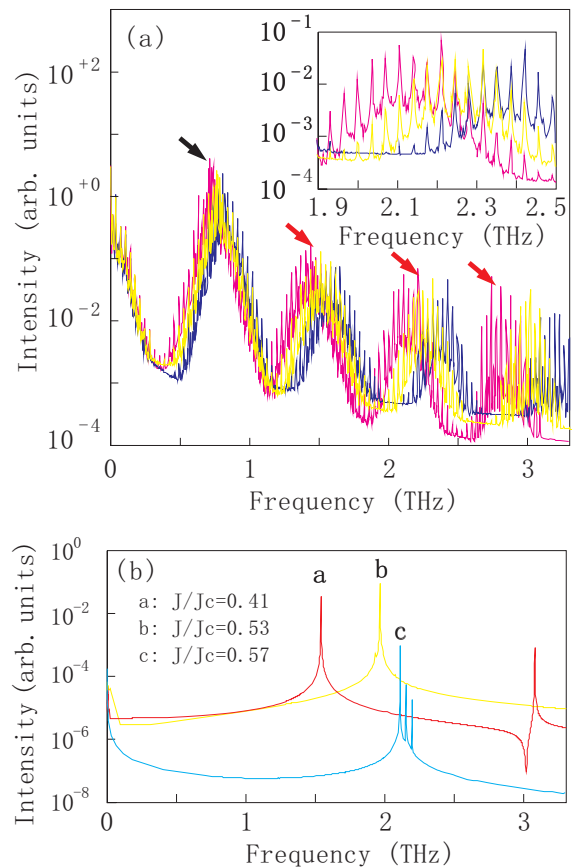


FIG. 4: (Color online). (a) The frequency spectra of the power. The external current are  $0.21J_c$  (pink),  $0.22J_c$  (yellow) and  $0.23J_c$  (blue). Arrows denote the major frequencies. The inset shows the enlarged view. (b) Frequency spectra of the power with high  $J_{ext}$ .

and lots of peaks appear. The envelope lines of these peaks have characteristic frequencies (black arrow) and higher harmonics (red arrows). These frequencies are generated from the  $\sin(\phi)$ . Integration of sine-Gordon equations gives  $\langle \beta \phi_t \rangle + \langle \sin(\phi) \rangle = J_{ext}$ , where  $\langle \beta \phi_t \rangle$  is the normal current and  $\langle \sin(\phi) \rangle$  is the supercurrent. As  $\langle \beta \phi_t \rangle$  is not zero, the base frequency of  $\sin(\phi)$  is derived

$$\frac{\langle \phi_t \rangle}{2\pi} = \frac{J_{ext} - \langle J_s \rangle}{2\pi\beta}. \quad (6)$$

The frequency, based on the external current, is of great importance to tune the supercurrent frequency. Furthermore, it can be used to control the radiation frequency and power.

Fig. 4(a) shows a discrete cavity resonance and an equidistant frequency difference. The phenomenon can be clearly seen in the inset, which is an enlarged view. It is also interesting to note that in the three lines for different external currents  $J_{ext} = 0.21J_c$  (pink),  $0.22J_c$  (yellow) and  $0.23J_c$  (blue), the peaks are in the same frequencies. It follows that these frequencies are intrinsic and independent of the external parameters, such as the external

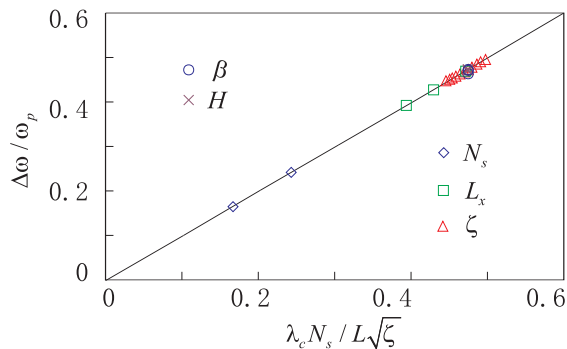


FIG. 5: (Color online). The intervals of the intrinsic frequencies. Only one of the parameters ( $N_s$ ,  $H$ ,  $L_x$ ,  $\zeta$  and  $\beta$ ) is changed in same group of data points.

current, the magnetic field, and so on. The differences ( $\Delta\omega$ ) between two neighboring frequencies could be regarded as the characteristic frequencies.

In order to clarify these intrinsic frequencies,  $\Delta\omega$  is calculated under different  $J_{ext}$ ,  $H_{ext}$ , length, layer number, and coupling  $\zeta$ . The results are divided into 5 groups and collected in Fig. 5. The parameters for the same group of data are fixed, except that one parameter denoted in the legend of Fig. 5 can be tuned. Because the frequencies are independent of  $\beta$  and  $H$ , the open circles and crosses with different  $\beta$  and  $H$  coincide. From this figure, we can observe that all data point can collapse onto a straight line described by  $\Delta\omega = \frac{N_s c}{L_x \sqrt{\zeta \epsilon_r}}$ . It follows that the intrinsic frequencies is  $\frac{n_x N_s c}{L_x \sqrt{\zeta \epsilon_r}}$ , where  $N_s = N_J + 1$  is the number of CuO layers and  $n_x$  is the natural number. Through observing the simulation data of the inner EM field, it could be found that  $n_x$  is the number of the standing wave nodes. On possible explanation for these phenomena is the EM resonance between  $z$  and  $x$  directions. The operator  $(1 - \zeta \Delta^{(2)})$  in Eq. (1) could be regarded as  $(1 - \partial_{z'}^2)$  with the dimensionless quantity  $z' = z_{eff}/\lambda_c$ , and the effective size  $z_{eff} = z \lambda_c / (s + D) \sqrt{\zeta}$ . The resonance occurs when  $\omega/k_x = \omega_z/k_{eff}$ .

For high external current, although the higher harmonics still exist, the frequency spectra of rectangular lattice is almost monochromatic, as shown in Fig. 4(b), close to

the experiment [15]. When the external frequency estimated by Eq. (6) equals to one of the intrinsic frequencies, the external current would excite a monochromatic resonance mode and the radiation would generate the maximum power, as denoted by the curves  $a$  and  $b$ . On the other hand, the external current would excite several resonance modes, when it is not equal to any intrinsic frequency, as shown by the curve  $c$ . The pink regime of Fig. (3) shows these resonance peaks with different  $J_{ext}$ . The distance ( $\Delta J_{ext}$ ) between two neighbor peaks is  $0.0098 J_c$ , consistent with the numerical result  $0.0093 J_c$  based on intrinsic frequencies.

For fields parallel to the  $ab$ -plane in BSCCO, vortices are periodically distributed. The distributions of supercurrent and the phase of the order parameter are also periodic. The normal current is no longer uniform, which results in periodical perturbation in the inner electric field. Therefore the vortices excite the alternative EM field. When the vortices are in motion, the alternative EM field is also propagating and decaying in BSCCO. In order to form a stable alternative EM field, the vortices and the EM field must move synchronously.

By increasing or decreasing the external current, the velocity of the flux flow is also changed. When  $J_{ext} < 0.47 J_c$ , the flux flow would move more slowly than the EM field. To achieve synchronies along the  $x$ -axis, the normal direction of the EM wavefront is not parallel to the flow direction. Because the boundary surface and the wavefront is not tangential, which weakens the power emission. On the other hand, when  $J_{ext} > 0.47 J_c$ , the external frequency would possibly resonate with the intrinsic frequencies, which pumps considerable energy into the inner alternative EM field. Since the boundary surface is tangential to the wavefront, the power emits much more efficiently.

The authors acknowledge useful discussions with X. Hu and S. Lin. This work was supported by National Natural Science Foundation of China under Grant No. 10774128, PCSIRT (Grant No. IRT0754) in University in China, National Basic Research Program of China (Grant Nos. 2006CB601003 and 2009CB929104).

\* Corresponding author. Email:qhchen@zju.edu.cn

- 
- [1] R. Kleiner, F. Steinmeyer, G. Kunkel, and P. Mller, Phys. Rev. Lett. **68**, 2394 (1992).
  - [2] H. B. Wang, P. H. Wu, T. Yamashita, Appl. Phys. Lett. **78**, 4010(2001); Phys. Rev. Lett. **87**, 107002(2001).
  - [3] B. Ferguson and X. C. Zhang, Nature Mater. **1**, 26 (2002).
  - [4] L. Ozyuzer *et al.*, Science **318**, 1291 (2007).
  - [5] M. Tachiki, M. Iizuka, K. Minami, S. Tejima, and H. Nakamura, Phys. Rev. B **71**, 134515 (2005).
  - [6] M.-H. Bae, H.-J. Lee, and J.-H. Choi, Phys. Rev. Lett. **98**, 027002 (2007).
  - [7] S. Lin, X. Hu, and M. Tachiki, Phys. Rev. B **77**, 014507 (2008).
  - [8] S. Savell'ev, A. L. Rakhmanov, and F. Nori, Phys. Rev. B **74**, 184512 (2006).
  - [9] T. Koyama, H. Matsumoto, M. Machida, and K. Kawakami, Phys. Rev. B **79**, 104522 (2009).
  - [10] A. E. H. Love, Phil. Trans. Roy. Soc. London (**A**)**197**, (1901).
  - [11] M. Machida, T. Koyama, A. Tanaka, and M. Tachiki, Physica C **330**, 85 (2000).
  - [12] M. Cirillo, N. Grønbech-Jensen, M. R. Samuelsen, M. Salerno and G. Verona Rinati, Phys. Rev. B **58**, 12377 (1998).

- [13] L. N. Bulaevskii and A. E. Koshelev, Phys. Rev. Lett. **97**, 267001 (2006).
- [14] A. E. Koshelev and I. Aranson, Phys. Rev. B **64**, 174508 (2001).
- [15] K. Kadowaki, H. Yamaguchi, K. Kawamata, T. Yamamoto, H. Minami, I. Kakeya, U. Welp, L. Ozyuzer, A. E. Koshelev, C. Kurter, K. E. Gray, and W.-K. Kwok, Physica C, **468**, 634, (2008).
- [16] M. Tachiki, S. Fukuya and T. Koyama, Phys. Rev. Lett. **102**, 127002 (2009).